We are IntechOpen, the world's leading publisher of Open Access books
Built by scientists, for scientists

4,800
Open access books available

122,000
International authors and editors

135M
Downloads

Our authors are among the

154
Countries delivered to

TOP 1%
most cited scientists

12.2%
Contributors from top 500 universities

WEB OF SCIENCE™

Selection of our books indexed in the Book Citation Index in Web of Science™ Core Collection (BKCI)

Interested in publishing with us?
Contact book.department@intechopen.com

Numbers displayed above are based on latest data collected.
For more information visit www.intechopen.com

Chapter 6

Structure Investigations of Rare-Earth Doped Nano-Particles – Extracted from Oxyfluoride Glass Ceramics by Thermal Induction and Corrosion Treatment

Hui Guo, Yu Hua, Lijuan Zhao and Yiming Li

Additional information is available at the end of the chapter

http://dx.doi.org/10.5772/57213

1. Introduction

Trivalent Lanthanide (Ln^{3+}) ions doped materials are well-known due to their superior luminescent properties and widely utilization in display field and fluorescent lights. Compared to organic fluorophores and semi-conducting nano-particles, Ln^{3+}-doped inorganic nano-particles have high photochemical stability, sharp emission bandwidths and large anti-Stokes shifts, therefore can be applied as excellent luminescence materials [1,2]. More recently, they also attract great interests as a new class of bioprobes, because their long-lived and intense emissions offer promising applications to biosensing, biological labeling and imaging technology [3-9]. Therefore, many researchers devote themselves to explore how to synthesize Ln^{3+}-doped inorganic nano-particles. Ever since the first report on oxyfluoride glass ceramics (GCs) [10], they have received great attention from many researchers due to the perfect mechanical stability and the efficient visible to infrared emission [11-14]. However, the luminescent nano-particles embedded in the bulk glass matrix can not be applied in mentioned fields directly, and how to free them from glass matrix is a problem to be solved. Unfortunately, there have been much research on the properties of nano-particles in GCs but no publication has been reported about how to obtain free and pure nano-particles into aqueous solution from the oxide glass matrix and how to apply it to the fields mentioned above, especially in biological field. Only Mortier and Patriarche [15] have reported an original way to synthesize single-crystal PbF_2 nano-particles used oxide GeO_2-PbO glass as the template and then the nano-particles were produced by dissolving the amorphous GeO_2-PbO phase of GCs with hydrofluoric acid. However, the corrosion reaction between the amorphous GeO_2-PbO and hydrofluoric acid can hardly be complete so that the obtained nano-particles had an amorphous phase as a shell in their experiment. Therefore, it is of great significance to develop

INTECH
open science | open minds

© 2014 Guo et al.; licensee InTech. This is a paper distributed under the terms of the Creative Commons Attribution License (http://creativecommons.org/licenses/by/3.0), which permits unrestricted use, distribution, and reproduction in any medium, provided the original work is properly cited.

convenient routes to fabricate inorganic nano-particles doped rare-earth (RE) ion in aqueous solution from GCs in order to meet their practical application requirements.

This chapter describes an innovative route to fabricate Ln^{3+}-doped nano-particles, with high efficient luminescent intensity and adjustable size, from oxyfluoride glass by the thermal induction and corrosion treatment [16]. Then the structure of obtained nano-particles can be investigated directly because optical properties of Ln^{3+} ions are very sensitive to the local environment [17,18] and Ln^{3+} ions are normally used as probes to survey the local structure in luminescent materials [19-23]. To determine the chemical composition of the obtained nano-particles accurately, energy dispersive X-ray spectroscopy (EDS) has been applied after getting rid off the interference of oxide glass matrix. X-ray diffraction (XRD) measurements were performed to identify the crystallization phases of nanocrystals with a power diffractometer (D/Max-2500), using CuKa as the radiation. To prove the structure of nano-particles, Rietveld analyses of XRD patterns were also carried out with the Fullprof program [24] or MAUD (material analysis using diffraction) program [25] in the range 10°-120° using the profile function of pseudo-voigt with axial divergence asymmetry. For the Rietveld analyses, the XRD data were acquired in the step-scan mode with a step of 0.02° (2θ) at a counting time of 1 s per step. High resolution transmission electron microscope (HRTEM) analysis was performed to observe the morphology of samples on a Philips TZOST TEM operating at 200kV. STEM and EDS line scan were performed on a Tecnai G2F30 field emission transmission electron microscope (FE-TEM) using HAADF as imaging mode. The emission spectra were recorded on an Edinburgh Instruments FLS920 spectrofluoremeter equipped with the continuous (450 W) xenon lamps.

2. Nano-particles preparation

The chemical compositions of the precursor glasses are shown in Table 1. About 20 g of raw materials were fully mixed and melted in a covered platinum crucible in air atmosphere at 1,000 °C for 2 h, and then cast into a steel plate [26-28]. To obtain nano-particles in glass ceramic, the glass samples were subsequently heat-treated at 470 °C for 8 h at the nucleation temperature measured by differential thermal analysis (DTA). Using DTA equipment (TA-Inst 2100), samples were held in a Pt crucible and analyzed against a calcined Al_2O_3 reference at a heating rate of 20 °C min^{-1}.

Compositions	Mole Fraction
SiO_2	50-y-x
Al_2O_3	y
PbF_2	40
CdF_2	10
RE_2O_3	x

Table 1. Compositions of the raw materials.

http://dx.doi.org/10.5772/57213

Figure 1(a) shows the XRD pattern of the investigated glass ceramics. After thermal induction, the XRD pattern of GCs presented intense diffraction peaks, which can be easily assigned to the β-PbF_2:Er^{3+},Yb^{3+} phase [29,30]. The lattice constant of β-PbF_2 crystal with the fluorite structure is a = 0.575nm. The slightly smaller lattice constant of the present nano-particles can be interpreted by that the nano-particles are a β-PbF_2 solid solution in which Pb^{2+} ions with ionic radius of 0.129 nm are partially substituted by RE-ion with ionic radius about 0.100nm [29]. This result is further supported by TEM of our GCs shown in Figure 1(b). The micrograph reveals that nano-particles are uniformly dispersed in the glass matrix. Furthermore, the particle size distribution has been shown in Figure 1(c). The average size of as-prepared nano-particles determined from TEM image is 42.6 nm.

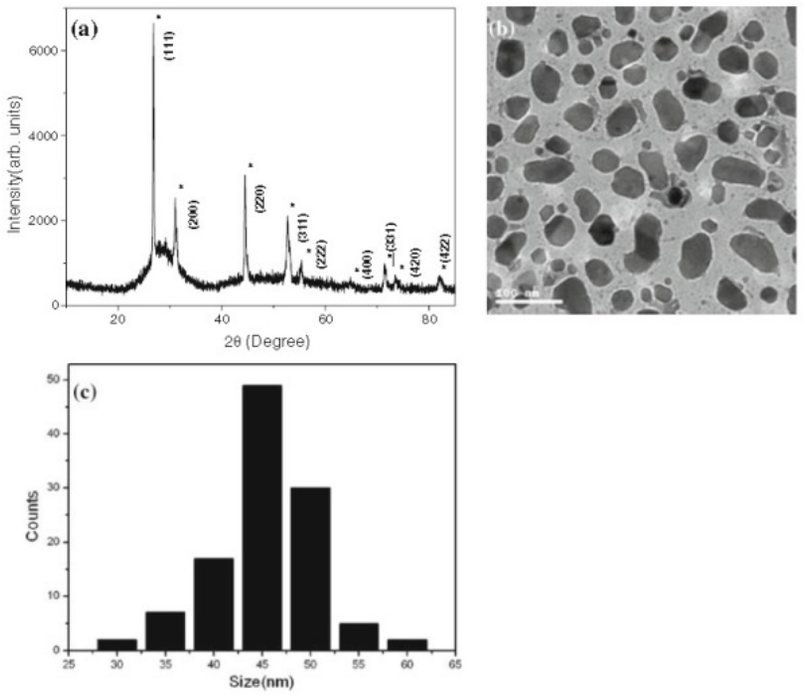

Figure 1. (a) XRD patterns of glass ceramics after thermal induction. The asterisks correspond to JCPDS file NO. 06-0251 (β-PbF_2). (b) TEM micrographs of nano-particles existing in glass matrix. (c) The size distribution of nano-particles in glass matrix [16]. Reproduced from Nanoscale Res. Lett., 2008, 3(12), 516. Copyright 2008, Springer.

To extract the nano-particles from the oxyfluoride glass ceramics, the corrosion treatment methods are as follows:

i. Firstly, the powder of GCs (about 500 mg) was immersed into 10.89 mol/L hydrofluoric acid. Then a benzene isolated layer was added to cover the hydrofluoric acid in the improved setting, as shown in Figure 2. Thus, corrosion reaction becomes more thorough and during the corrosion process, the benzene-blocking-layer separates the reactants and the air atmosphere, which is able to avoid oxidation efficiently.

ii. Secondly, the mixed solution was stirred for about 20 h to get rid off silicate glass matrix with the formula of $SiO_2 + 4HF = SiF_4\uparrow + 2H_2O$. After corrosion treatment, the

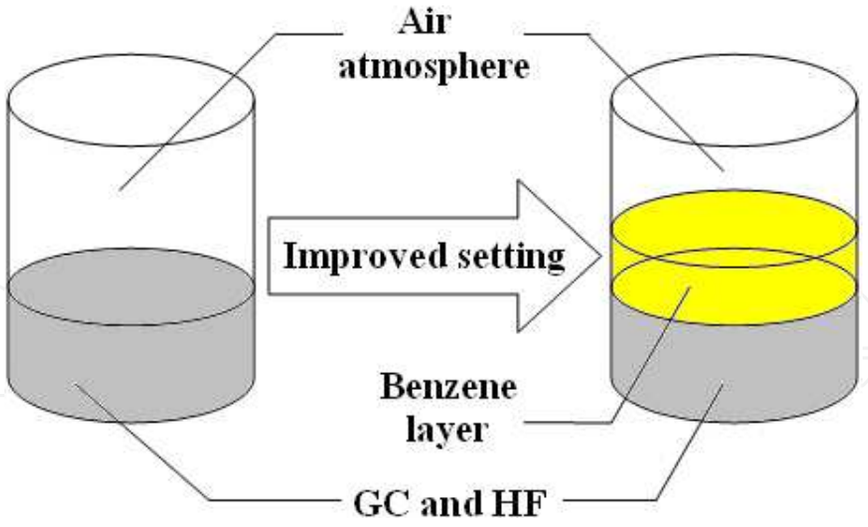

Figure 2. A general description of the corrosion process design.

nano-particles were deposited by solid-liquid separation. Then pH value was adjusted to neutrality by repeated adding distilled water.

iii. Finally, the nano-particles in aqueous solution were dispersed using sodium lauryl benzenesulfate and vacuum dried at 65 °C for 24 h to acquire the powder of nano-particles.

As shown in Figure 3, XRD spectra and TEM image of the obtained nano-particles after corrosion treatment are presented. Phase identification of the nano-particles has been studied by using XRD. The typical XRD patterns show strong diffraction peaks that can be indexed to the β-PbF_2:Er^{3+},Yb^{3+} phase due to the appreciably shift of XRD peaks position and former research results. No additional or intermediate phase is detected in the sample. The peaks position and half peak breadth of XRD are in concordance with those measured in GCs, which indicates that nano-particles are released from glass matrix to aqueous solution. Moreover, the baseline of XRD is nearly a straight line compared with that of XRD of GCs, which also indicates that silicate glass host is corroded completely. The Figure 3(b) is the TEM image of nano-particles in aqueous solution and Figure 3(c) reveals the size distribution. The average particle size is obtained as 41.7 nm, which is very close to the former calculation result of nano-particles existing in glass matrix 42.6 nm. And the comparison of Figure 1 and Figure 3 indicates that the nano-particles formed in glass matrix are released to aqueous solution and their structure, shape and size distribution in glass host are kept well. The potential reason could be the restriction of glass network structure during the thermal induction process. The nano-particles exhibit a narrow size distribution and display a good dispersibility in aqueous solution.

To illustrate the luminescent properties of the nano-particles can be kept after corrosion treatment, Figure 4 reveals the main up-conversion (UC) emission of the $^2H_{11/2}/^4S_{3/2}/^4F_{9/2} \rightarrow {}^4I_{15/2}$ transition in GCs and in aqueous solution under 980nm diode laser excitation. The weak ultraviolet UC radiation of the $^4G_{11/2} \rightarrow {}^4I_{15/2}$ transition were not shown here, since we focus on the ratio of red and green fluorescent intensities, which could show the variation of crystal

http://dx.doi.org/10.5772/57213

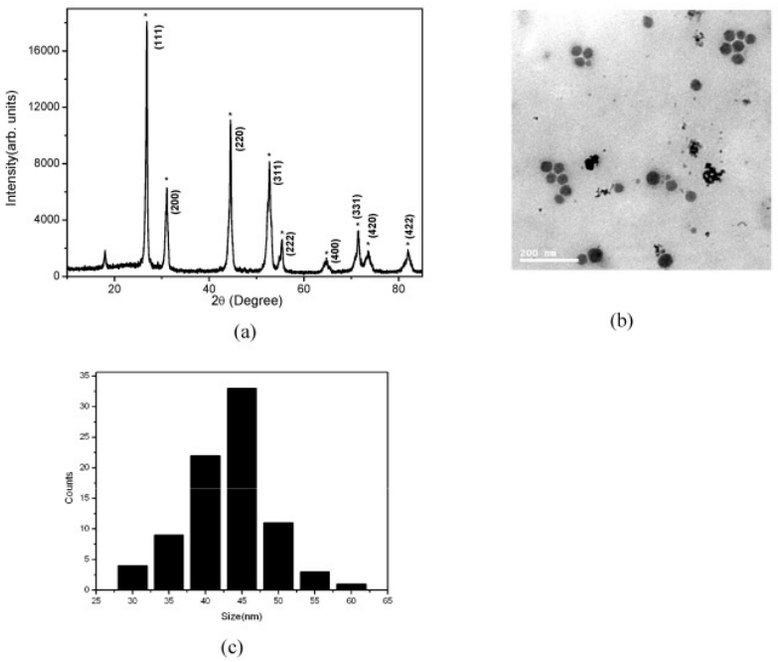

Figure 3. (a) XRD patterns of glass ceramics after thermal induction. The asterisks correspond to JCPDS file NO. 06-0251 (β-PbF_2). (b) TEM micrographs of nano-particles existing in glass matrix. (c) The size distribution of nano-particles in glass matrix [16]. Reproduced from Nanoscale Res. Lett., 2008, 3(12), 516. Copyright 2008, Springer.

lattice field around the RE-ion. Compared to GCs, the red fluorescence intensity of nano-particles in aqueous solution dramatically increases. The UC mechanisms of the green and red emissions had been researched by our groups [30]. And the Er^{3+} ion can be promoted to the $^4I_{11/2}$ state through ground state absorption (GSA) of laser photons, and then to the $^2H_{11/2}$ state by use of the excited state absorption (ESA) or energy transfer UC (ETU) processes. The $^4S_{3/2}$ state can also be populated by relaxations from the upper $^2H_{11/2}$ state. The green luminescence is emitted by the transition from $^2H_{11/2}$ and $^4S_{3/2}$ state to $^4I_{15/2}$ ground state. Hence, the green UC luminescence seldom subjects to influence of phonon energy difference of crystal field around the RE ions. The red UC luminescence, however, comes from the phonon-assisted quantum cutting (PQC) process, which primary generated in low phonon energy crystal lattice field. It is worthwhile to point out that luminescent signal include emission from RE ions in glass host and fluoride nano-particles at luminescent spectra. In GCs, most of RE ions are incorporated in the fluoride crystal phase, which mainly emit red UC luminescence. Nevertheless, a part of RE ions exists in glass host and mainly emits green UC luminescence. As Figure 4 shows, the ratio value of red and green UC luminescent intensities increase from 1:1.31 in glass ceramics to 1:0.61 in nano-particles aqueous solution. The key reason for the red UC enhancement arises from the fact that the glass host is corroded by hydrofluoric acid, the fluoride nano-particles formerly embedded in glass matrix are released to aqueous solution and eventually red UC luminescent intensities increase sharply. These results are consistent with the conclusion drawn by XRD and TEM. The nano-particles in aqueous solution have the same luminescent properties as them existing in glass host.

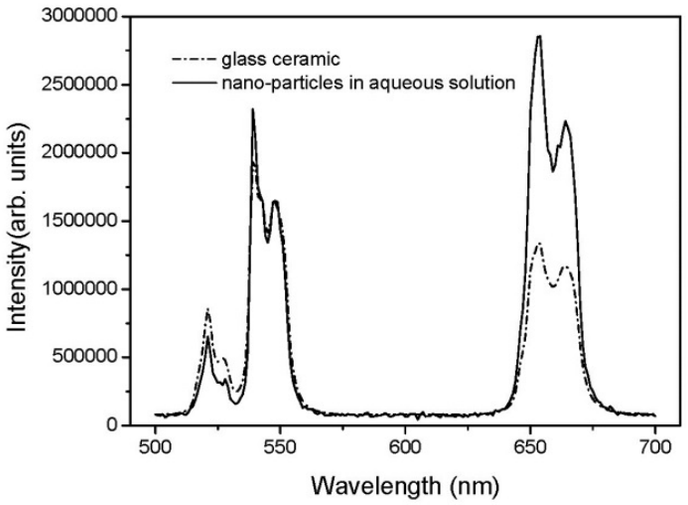

Figure 4. UC red and green emissions of GCs and nano-particles in aqueous solution under diode laser excitation of 980 nm [16]. Reproduced from Nanoscale Res. Lett., 2008, 3(12), 516. Copyright 2008, Springer.

In conclusion, the nano-particles can be extracted from glass matrix by the mentioned thermal induction and corrosion treatment. Their structure and luminescent properties can be kept as well. However, although the preparation method is based on a fundamental consideration, our proposed corrosion treatment has its limitations: (i) the matrix that need be corroded can react with the hydrofluoric acid, in general, they are some oxide compounds; (ii) the nano-particles can not react with the hydrofluoric acid, in general, they are some fluoride nanocrystals such as PbF_2, CaF_2, BaF_2, $NaYF_4$, and so on. But notably, these RE-doped fluoride nano-particles attract much more attention compared with oxide nano-particles because of their low phonon frequency. Therefore, our proposed corrosion treatment can be applied widely to any other eligible systems.

3. Structure investigations of the obtained nano-particles

In general, the optical properties of Ln^{3+} ions are very sensitive to the local environment, and especially the emission intensity of Ln^{3+}-doped materials are closely correlated with the surrounding crystal-field [18,31]. Therefore it is of primary importance to identify the structure of nano-particles in rare-earth doped GCs [32,33]. However, from $Cd_xPb_{1-x}F_2$ model to $Pb_{1-x}Er_xF_{2+x}$ model, most of structural investigations of nano-particles in GCs are indirect due to the effect of the glass matrix. The quantitative tetragonal structure has been proposed directly until the corrosion treatment method has been reported. Based on corrosion treatment, additionally, the distribution of different RE ions in GCs can also be determined clearly. Some proposed structure models in different stage are summarized in Table 2 below. And then, the distribution of different RE ions in GCs is discussed detailed in parts 3.1 and 3.2.

Glass Matrix	Doped ions	Do corrosion treatment or not	Structure of Nano-particles	Refs.
SiO_2-Al_2O_3	Pr^{3+}, Er^{3+}, Yb^{3+}	Not	$Cd_xPb_{1-x}F_2$	[10,11]
SiO_2-Al_2O_3	Er^{3+}	Not	β-PbF_2:Er^{3+}	[34]
GeO_2-PbO	Er^{3+}	Not	β-PbF_2:Er^{3+}	[35,36]
SiO_2-Al_2O_3	Er^{3+}	Not	$Pb_{1-x}Er_xF_{2+x}$	[26]
-- --	Nd^{3+}, Eu^{3+}, Er^{3+}	Not	$Pb_{1-x}Er_xF_{2+x}$	[37]
SiO_2-Al_2O_3	Eu^{3+}	Not	Tetragonal	[33]
SiO_2-Al_2O_3	Er^{3+}, Yb^{3+}	Do	Tetragonal $PbREF_5$	[24]
SiO_2-Al_2O_3	Nd^{3+}	Do	Core-shell structure	[25]
SiO_2-Al_2O_3	Yb^{3+}, Tb^{3+}, Tm^{3+}, *et al*.	Not	Cubic Pb_3REF_9 and Tetragonal $PbREF_5$	[38]

Table 2. Different proposed structure models of nano-particles in glass ceramics systems.

3.1. Distribution of heavy RE ions and the tetragonal structure proposed

Oxyfluoride glass with composition (mol%) of $30SiO_2$-$15.5Al_2O_3$-$40PbF_2$-$10CdF_2$-$0.5Er_2O_3$-$4Yb_2O_3$ was thermal treated by 460 °C, 480 °C, 500 °C, 520 °C, 540 °C, 560 °C and subsequently cooled to room temperature to be GCs (labeled as GC@460 °C, GC@480 °C, *etc.*). Afterwards, corresponding nanocrystals (NCs) (labeled as NC@460 °C, NC@480 °C, *etc.*) were obtained by corrosion treatment mentioned above [16]. For samples of Pb/Cd = 40/10, the EDS measurement of the NCs presents that at% of NCs is Pb:RE:F = 1.06:1:4.99, which is very close to the stoichiometric proportion 1:1:5. These indicate that RE ions are incorporated into fluoride nano-particles during thermal treatment. GC samples which are thermal treated at different temperatures remain essentially the same proportion. The detected trace of Cd in EDS up to only 0.09 at% indicates that the nano-particles is RE^{3+} doped β-PbF_2 (here RE^{3+} = Er^{3+} or Yb^{3+}), rather than $Cd_xPb_{1-x}F_2$. And even the trace of Cd in EDS of samples of Pb/Cd = 25/25 is only 0.19 at%. The same low atomic concentration confirms that Cd hardly congregated into the nanocrystals, which is basically independent of the initial content of Cd in raw materials. This RE^{3+} doped β-PbF_2 composition has been accepted by more and more researchers in the past decade [26,39,40].

Figure 5 shows the XRD patterns of the GCs as made. After crystallization, several diffraction peaks are exhibited. Apparently, XRD patterns are divided into two groups by the shape of peaks as: one is low temperature group (460 °C, 480 °C, 500 °C) and the other is high temperature group (520 °C, 540 °C, 560 °C). Some peaks of XRD corresponding to high temperature group split quite obviously compared with those corresponding to low temperature group. Since the chemical composition acquired from EDS of all these samples is almost the same and the sum of relative intensities of the splitting XRD peaks is basically equal to the relative intensities of the corresponding peaks which do not split, we believe that the basic structures of crystals of the two groups should be similar in general.

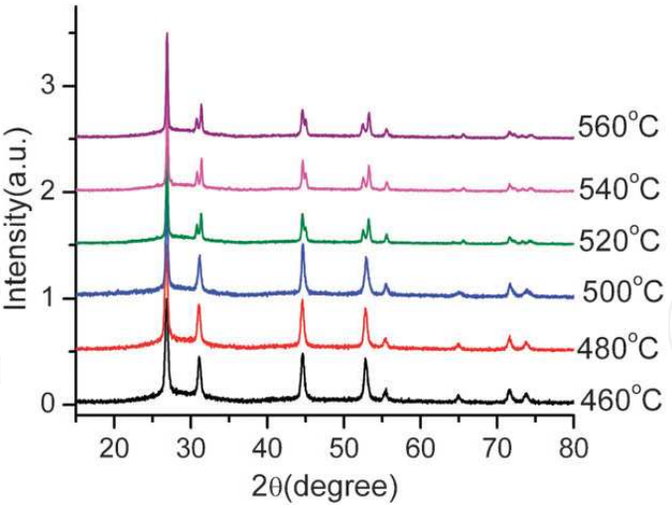

Figure 5. X-ray diffraction patterns of GCs obtained from the oxyfluoride glasses after thermal treatments at different temperatures [24]. Reproduced from Phys. Chem. Chem. Phys., 2011, 13(4), 1499. Copyright 2011, Royal Society of Chemistry.

The conclusion that the most commonly found trivalent RE site in CaF_2 is one of tetragonal C_{4v} (*4mm*) crystal-field symmetry. Since β-PbF_2 has a structure of CaF_2 (*i.e.*, fluorite structure), the formation mechanism of RE^{3+} doped crystal is clearly alike. Additionally, Beggiora *et al.* have proved that the F^- interstitial mechanism is energetically more favorable than Pb vacancy compensation as a charge compensation mechanism by computer simulation methods [26]. Mainly based on the points above, we put forward the structure displayed in Figure 6. RE^{3+} is substituted for Pb^{2+} at the center of the tetragonal lattice with four more interstitial F^- ions residing in the midpoint of the edges besides the original eight F^- in fluorite structure. This structure has a typical D_{4h} (*4/mmm*) point symmetry, which results in a higher symmetry, but includes all the symmetry operations of C_{4v} (*4mm*). The space group corresponds to *P4/mmm* (NO.123). Site symmetries and other atomic parameters are listed in Table 2 ("Ox." and "Wyck." are short for the oxidation number and the Wyckoff letter, respectively).

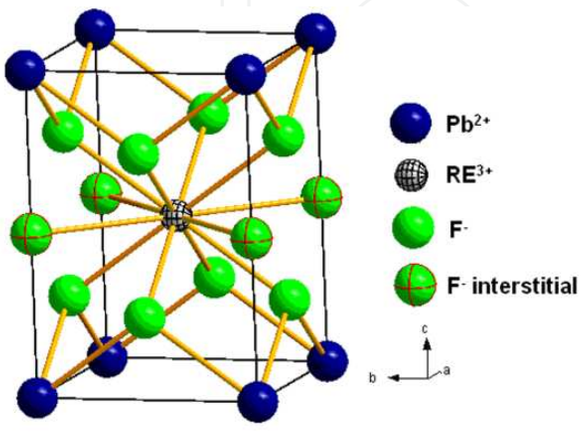

Figure 6. Stereoscopic view of structure of nano-particles embedded in glass ceramic [24]. Reproduced from Phys. Chem. Chem. Phys., 2011, 13(4), 1499. Copyright 2011, Royal Society of Chemistry.

http://dx.doi.org/10.5772/57213

Atom	Ox.	Wyck.	Site symmetry	x/a	y/b	z/c
Pb	2	1a	*4/mmm*	0	0	0
Yb	3	1d	*4/mmm*	1/2	1/2	1/2
F	-1	4i	*2/mm.*	0	1/2	1/4
F interstitial	-1	1b	*4/mmm*	0	0	1/2

Table 3. Atomic parameters of the structure model (Space-group:*P4/mmm* (NO.123)-tetragonal). Adapted from Ref. [24].

XRD patterns of the six GC samples as made were compared with the theoretical calculation by program Diamond 3.1d based on the structure proposed above. For high temperature group samples, take GC@540 °C for example, as shown in Figure 7(a), the lattice parameters were set as a = 4.026 Å, c = 5.793 Å. Since the calculation results can only be expressed as the form of vertical bar theoretically (see vertical bars in Figure 7(a), lower panel), the XRD trace (raw data) was converted to the form of integral intensities of peaks (*i.e.*, the peak area value, see vertical bars in Figure 7(a), upper panel) in order to compare with the theoretical results. Indexing according to the tetragonal model was also taken as exhibited in Figure 7(a), lower panel. As seen from Figure 7(a), the positions and integral intensities of peaks derived from experiment are consistent very well with those calculated based on the tetragonal model. Quantitative calculation indicates that the average relative errors between theoretical and experimental values are only 0.052 % and 2.363 % in 2θ and relative intensity for every peak, respectively.

Much the same, with GC@480 °C as the representative, Figure 7(b) shows the compared XRD data of the low temperature group samples. With the indexing of tetragonal, lattice parameters were set as a = 4.065 Å, c = 5.749 Å. Calculated average relative errors between theoretical and experimental values are only 0.068 % in 2θ and 2.199 % in relative intensity for every peak, respectively. These results quantitatively support the proposed structure.

To further confirm the validity of the proposed structural model, the XRD refinements of the NCs were made by the Rietveld method with the Fullprof program. Based on the Lattice parameters and the atomic coordinates adopted above, the scaling factors, zero corrections and peak shape parameters (including FWHM, asymmetry and pseudo-Voigt profile functions) were deduced. Figure 8(a) and Figure 8(b) show the final Rietveld plot of GC@480 °C and GC@540 °C respectively. Although the envelope lines due to the existing of glassy matrix and peaks broadening due to the small size of the nano-particles exert a serious impact on the results of fitting, the corresponding factors R_p(= 7.86%), R_{wp}(= 10.6%) for GC@480°C and R_p(= 8.76%), R_{wp}(= 12.4%) for GC@540 °C indicate a relatively good agreement between the experimental and calculated patterns.

3.2. Distribution of light RE ions and the core-shell structure

Precursor glasses (PGs) with the composition $44SiO_2$-$5Al_2O_3$-$40PbF_2$-$10CdF_2$-$1NdF_3$ (mole fraction) were prepared by traditional melting-quenching method. With the prepared precursor glasses, the corresponding transparent GCs were obtained by thermal treatment for 48

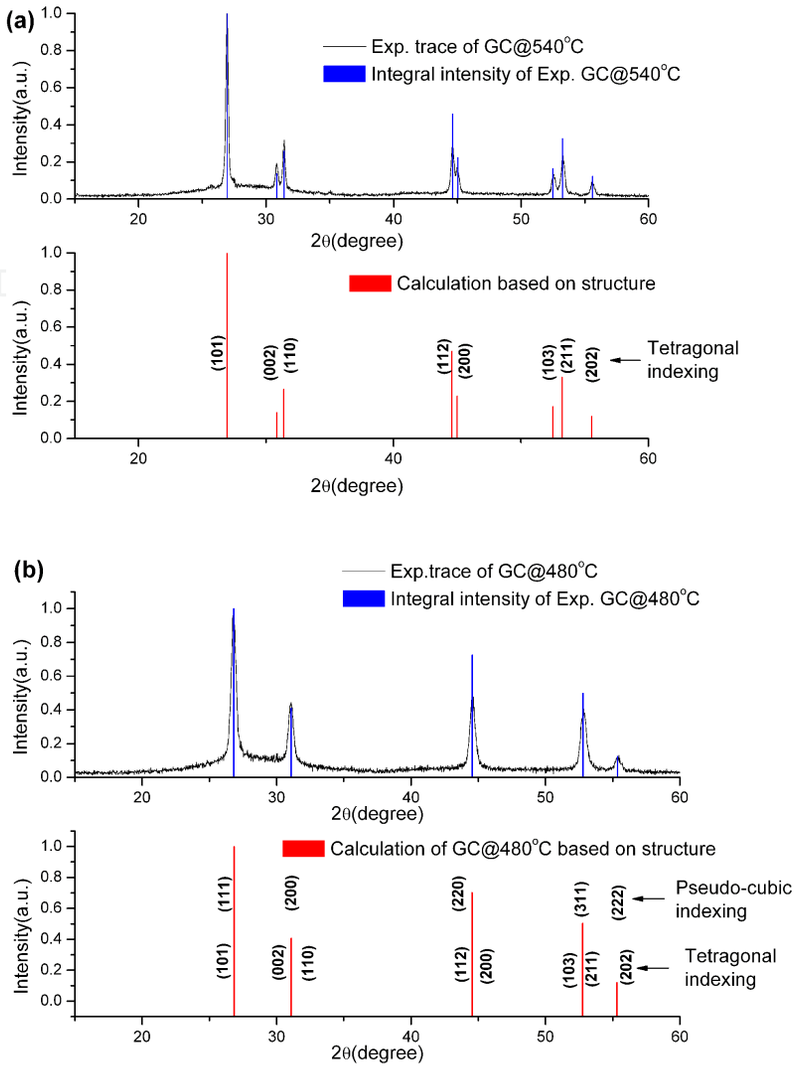

Figure 7. Quantitative comparison of theoretical and experimental X-ray diffraction patterns of glass ceramics thermal treated at (a) 540 °C and (b) 480 °C [24]. Reproduced from Phys. Chem. Chem. Phys., 2011, 13(4), 1499. Copyright 2011, Royal Society of Chemistry.

hours at 440 °C, which is determined by differential thermal analysis (DTA). With corrosion treatment, the corresponding fluoride nano-particles were obtained afterwards [16].

Figure 9(a) shows the diffraction patterns of compounds of GCs, along with the diffraction pattern of PGs without thermal treatment. Two curves show an overlap of the peaks corresponding to the amorphous matrix of Si-Al glass. The differences between PGs and GCs indicate that the crystallization process takes place in glass matrix under thermal treatment, and the characteristic diffraction peaks of pure cubic β-PbF_2 (JCPDS: 06-0251) emerge. XRD patterns of the GCs were compared with the theoretical calculation by program Diamond 3.1d based on the structure of pure cubic β-PbF_2. Since the calculation results can only be expressed in the form of a vertical bar theoretically (see vertical bars in Figure 9(c)), the XRD trace (raw data) was converted to the form of integral intensities of peaks (i.e., the peak area value, see

http://dx.doi.org/10.5772/57213

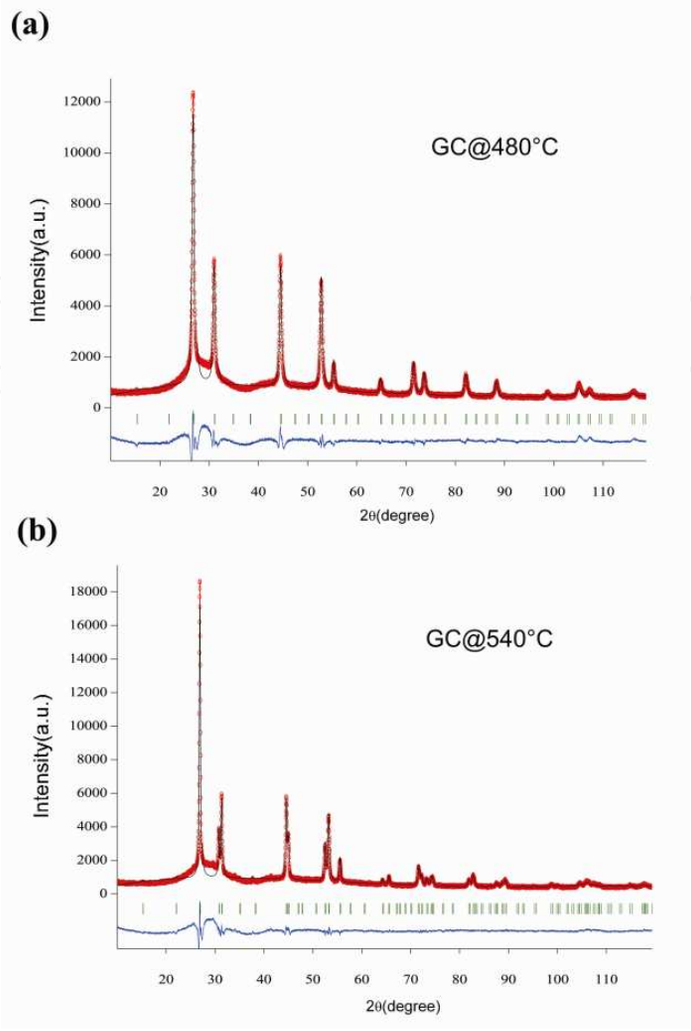

Figure 8. Rietveld analyses for X-ray diffraction patterns of (a) GC@480 °C and (b) GC@540 °C. The positions of the Bragg reflections are indicated by vertical bars (|). The difference between the experimental (small circles) and the calculated (solid line) intensities from the model is shown by the plot in the lower part of the diagram [24]. Reproduced from Phys. Chem. Chem. Phys., 2011, 13(4), 1499. Copyright 2011, Royal Society of Chemistry.

vertical bars in Figure 9(b)) in order to compare with the theoretical results. Indexing was also taken as exhibited in Figures 9(b) and (c). As seen in Figures 9(b) and (c), the positions and integral intensities of peaks derived from experiment are very consistent with the calculation based on the structure of pure cubic β-PbF_2. Quantitative calculation indicates that the average relative errors between the theoretical and experimental values are only 0.98% and 4.37% in 2θ and the relative intensity for every peak, respectively. In order to further confirm the validity of the nanocrystals structure, pure cubic β-PbF_2, X-ray data refinement was made using the program MAUD. The analysis was started assuming the structure of β-PbF_2 (F_{m3m} NO. 225) for the nanocrystal phase; and the structure of cubic amorphous silica-Al glass (P_{213} NO. 198) for the amorphous phase. The used crystalline structures can all be found in the database of the MAUD program. The corresponding factors R_{wp} (= 4.69%), R_{exp} (= 4.27%) indicate a relatively good agreement between the experimental and calculated patterns.

According to the results of obtained quantitative analysis, about 8.6 mol% to 13.5 mol% of the original Pb would contribute to form crystalline β-PbF_2 during the thermal treatment. In addition, the structure cell parameter of nanocrystal phase corresponds to that of pure cubic β-PbF_2, which further checks the structure of nanocrystal phase.

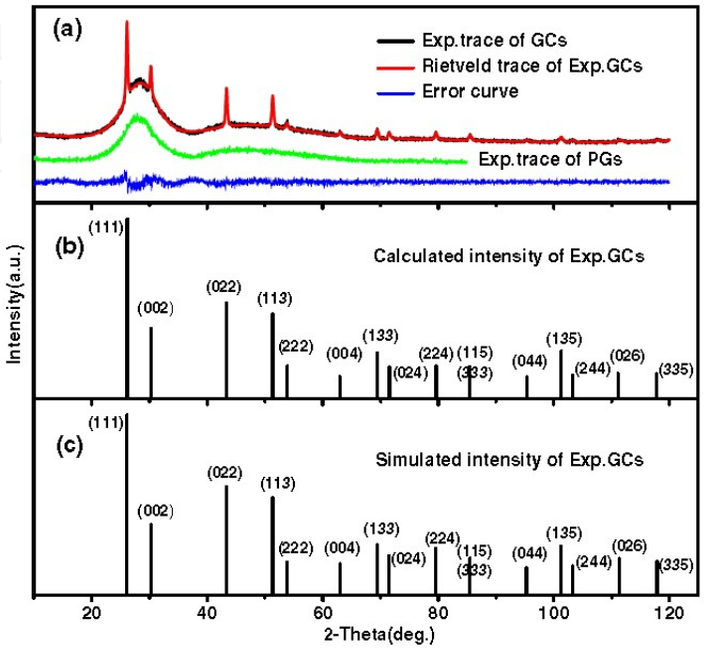

Figure 9. (a) X-ray diffraction patterns of GCs and PGs, Rietveld analyses for XRD pattern of GCs and the error curve. The calculated line spectrum from peak area of GCs (b) and the simulated line spectrum of GCs from Diamond program (c) are presented for comparison [25]. Reproduced from Nanoscale Res. Lett., 2012, 7(1), 275. Copyright 2012, Springer.

The Nd^{3+} ions could not be incorporated into nanocrystal phase by reason that the structure of nanocrystal phase is pure cubic β-PbF_2. Corrosion-treated methods were applied to acquire the NCs so as to explore the information on chemical compositions and structures of NCs and weaken the interference of glass matrix. For Nd^{3+}-doped samples, an unusual change happens when the nanocrystals embedded in glass matrix abstracted by etching process. Unlike our pervious work [24] of Er^{3+}/Yb^{3+}-codoped GCs that only β-PbF_2 phase was observed, the complex mixture were obtained after etching off the glass matrix of GCs doped with Nd^{3+}. With peak indexing, the additional intense diffraction peaks appear to be NdF_3 (JCPDS: 09-0416) and Pb_3AlF_9 H_2O phase (JCPDS: 45-1458). The new crystal phase NdF_3 generates in the course of the etching treatment, namely Nd^{3+} ions existed in glass matrix reacting with F^- ions in acid generates NdF_3. Likewise, Pb and Al ions of glass matrix reacting with F^- ions in acid generates Pb_3AlF_9 H_2O phase. MAUD program based on Rietveld method was used to calculate the relative amounts of β-PbF_2 and NdF_3 phases. The crystal structure information of the concerned phases is acquired from the Crystallography Open Database (http://www.crystallography.net/). The refinement results and difference plot for the observed and calculated patterns of NPs are shown in Figure 10. The refining factors of R_{wp} (= 8.07%) and R_{exp} (= 4.02%) indicate a good agreement between the experimental and calculated patterns.

http://dx.doi.org/10.5772/57213

The structure cell parameter of β-PbF_2 obtained from refinement of NCs (0.5890 nm) and GCs (0.5898 nm) is nearly the same as that of pure β-PbF_2 (0.5927 nm), which further verifies the existence of Nd^{3+} outside the NCs. According to the else relative results obtained from Rietveld analysis, the cell parameters of the other two phases are nearly the same as that of the standard structures separately, which further certifies the authenticity of the complex phases suggested above. From the results of the relative weight fraction obtained from refinement, moreover, through the sample arithmetic conversion, we can acquire that about 10.9 mol% the Pb of raw material contribute to form crystalline β-PbF_2 phase during the thermal treatment. This conclusion is in accordance with Rietveld analysis data from Figure 9.

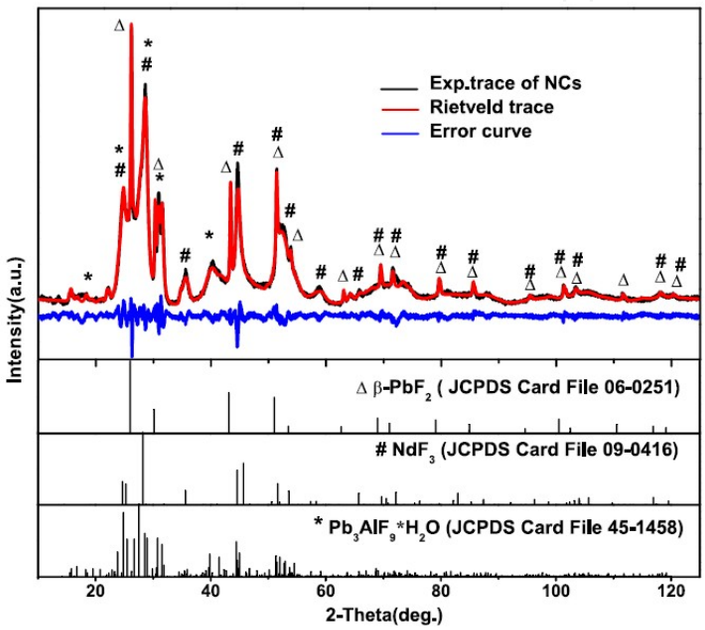

Figure 10. Rietveld analyses for XRD pattern of NCs and the error curve are presented. The line spectrum of β-PbF_2, NdF_3 and Pb_3AlF_9 H_2O are revealed for comparison [25]. Reproduced from Nanoscale Res. Lett., 2012, 7(1), 275. Copyright 2012, Springer.

High resolution TEM micrographs of GCs and NCs are displayed in Figure 11, providing a visual characterization of the samples and a directly analysis method. In GCs, as shown in Figure 11(a), only spherical β-PbF_2 nanocrystals with an average size about 22 nm distribute in glass matrix, which has a good consistency with the calculated size by using the Scherrer formula. However, in NCs, besides the 22 nm-nanocrystals already existed in GCs, as shown in Figure 11(b), a large amount of additional crystals and flake-like substrates also emerge. Particularly, most of these additional crystals assemble around the known β-PbF_2 nanocrystals, forming a core-shell-like structure. According to the HRTEM micrographs, the periodic arrayed crystal planes can be viewed clearly and part of symbolic interplanar distance (*d*) values, which measured accurately for both GC and NCs, have been labeled. The measured values of *d*, 0.294nm or 0.295nm for both Figures 11(a) and (b), are attributed to crystal plane (002) of pure cubic β-PbF_2 that as the core, while the *d* values 0.303nm and 0.316nm around β-PbF_2 nanocrystal belong to crystal planes (020) and (-121) of shell NdF_3 respectively, and the

other one *d* value 1.141nm is for the symbolic crystal plane (001) of the substrates $Pb_3AlF_9\,H_2O$. This conclusion is in accordance with the XRD refinement result of NCs, which has been displayed in Figure 10 above. On the basis of Rietveld refining results and HRTEM micrographs, the Nd^{3+} ions are reserved in glass matrix after thermal treatment and aggregated outside β-PbF_2 particles in the form of NdF_3 crystals when glass matrix are removed through the etching process. Therefore, a simplified model is proposed to describe the distribution of Nd^{3+} ions both in GCs and NCs, as shown in the insets of Figures 11(a) and (b). That is to say, with thermal treatment on PGs, the phase segregation process happens and on the one hand, as shown in the inset of Figure 11(a), Nd^{3+} ions with a inhomogeneous distribution form an aggregate structure, which has been reported on previous research [41,42], on the other hand Pb and F element get together to form high temperature phase β-PbF_2 nanocrystals, while the formation of Nd^{3+} clusters prevents the process of incorporation into β-PbF_2 phase. During the etching process for removing glass matrix, the Nd^{3+} ions meet F^- ions in the acid solution and generate NdF_3 crystals. And then the large quantities of NdF_3 crystals adsorb the surface of the β-PbF_2 nanoparticles. The model for NCs is simplified as a core-shell structure for further analysis, viz. β-PbF_2 particle as core and the covering NdF_3 crystals as shell, as shown in the inset of Figure 11(b). This rough simplification is acceptable considering the quantitative analysis result of NCs.

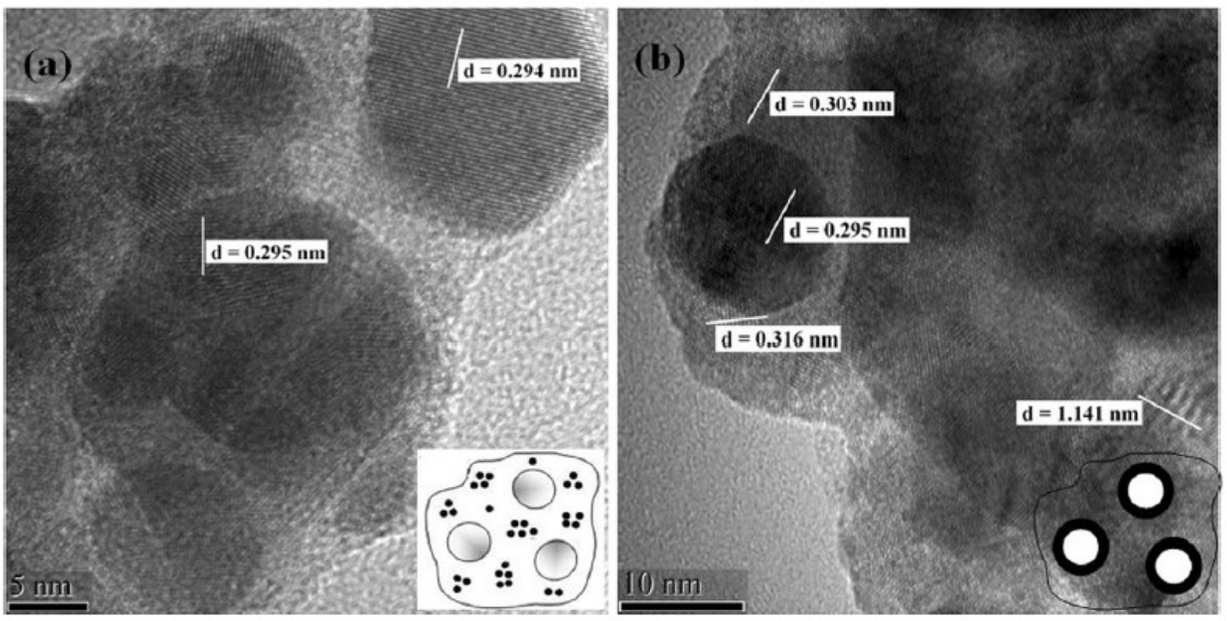

Figure 11. High resolution TEM micrographs with the marked interplanar distance *d* values of GCs (a) and NCs (b). The insets are the simplified models for GCs and NCs, where the large white spheres stand for β-PbF_2 nano-particles and small black spheres in GCs are for Nd^{3+} ions [25]. Reproduced from Nanoscale Res. Lett., 2012, 7(1), 275. Copyright 2012, Springer.

In order to verify the anticipation, EDS line scans in HAADF mode across the β-PbF_2 particles are carried out on a Tecnai G2F30 FE-TEM to offer signal intensity values for different elements. The line scanning paths are shown in Figures 12(a) and (b) and the results are shown in Figures

http://dx.doi.org/10.5772/57213

12(e) and (f). In GCs, the detected trace of Nd in EDS like that of Cd indicates that nanocrystalline phase is pure β-PbF_2, rather than β-PbF_2:RE, as previously suggested by many researchers. Even the trace of Nd in EDS of the other samples doped different concentration of Nd, the former researches confirmed that Cd hardly congregated in the nanocrystals, which also indicated that none of Nd ions were incorporated into β-PbF_2 crystalline phase [24,26,39]. Figure 12(c) shows EDS line scan for the ideal spheric body model of crystalline β-PbF_2 in GCs. As an ideal sphere model, dot *A* is for the center of it. Axial direction (*Z*) is the orientation of EDS line scan. Dot *O* and length *x* are the initial point and the distance of line scan separately. From Figure 12(c), we can get the relation formula the content of Pb satisfies:

$$Y_1 \propto 2\sqrt{R^2 - (R-x)^2} \tag{1}$$

Where Y_1 is the relative intensity of element Pb, *R* is the half size of β-PbF_2 nanocrystal and *x* is the length of line scan. Through conventional mathematical analysis, simulated curve is shown in Figure 12(e), which is in accordance with the fitting curve of experimental measurement. In the same way, the ideal core-shell structure model of NCs, which is shown in Figure

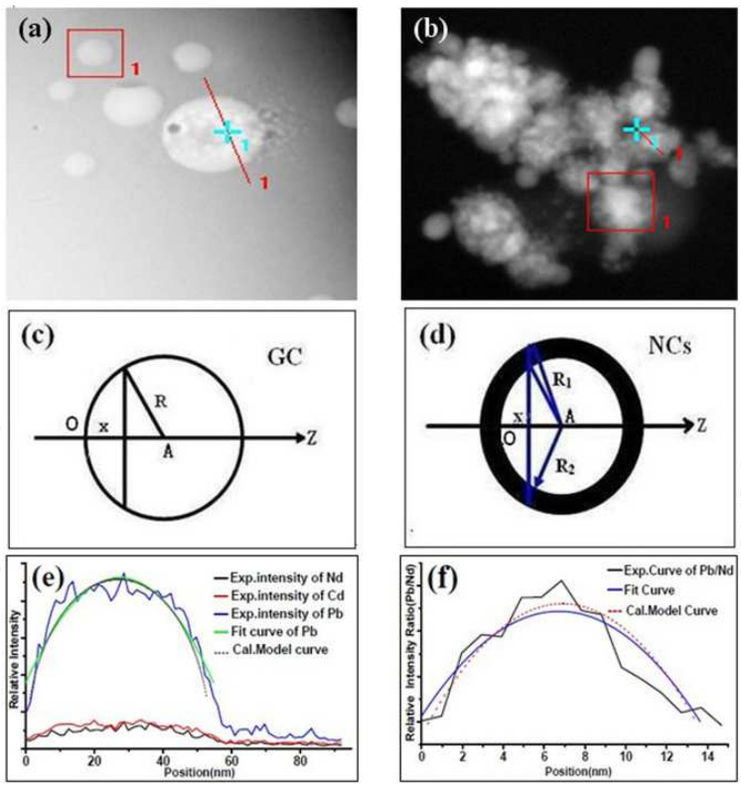

Figure 12. EDS line scan graphs in HAADF mode (a) and (b); The two pictures (c) and (d) are EDS line scan for the ideal models of crystalline β-PbF_2 and core-shell structure in NCs, respectively; The relative element signal intensity of Pb, Nd and Cd in GC, the fit curve and the calculated model curve of element Pb are presented for comparison (e); The fit curve of relative element intensity ratio Pb/Nd in NCs and the calculated core-shell model curve are also showed (f) [25]. Reproduced from Nanoscale Res. Lett., 2012, 7(1), 275. Copyright 2012, Springer.

12(d), is analyzed by conventional mathematical simulation, as shown in Figure 12(f). From Figure 12(d), the signal intensity ratio of the content of Pb and Nd can be expressed by following formula:

$$Y_2 \propto \frac{\sqrt{R_2^2 - \left(R_2 - x\right)^2}}{\sqrt{R_1^2 - \left(R_2 - x\right)^2} - \sqrt{R_2^2 - \left(R_2 - x\right)^2}} \tag{2}$$

Where Y_2 is the relative element intensity ratio Pb/Nd, R_1 and R_2 is the half size of core-shell model and β-PbF_2 nanocrystal respectively, and x is the length of line scan. The accordance with experimental results, as shown in Figures 12(e) and (f), proves the rationality of the model. Therefore, it is concluded that all of the Nd^{3+} ions locate in glass matrix, while few of the Nd^{3+} ions dope into crystalline phase.

4. Conclusions

An innovative route to fabricate nano-particles from oxyfluoride glass by the thermal induction and corrosion treatment was described. Although thermal induction and corrosion treatment were used to prepare β-PbF_2:RE^{3+} nano-particles in aqueous solution in this chapter, it may directly apply to any other silicate glass ceramics doped with other RE ions and embedded various composition of nano-particles, since the preparation method is based on a fundamental consideration. After obtaining the free and pure nano-particles, the structure of nano-particles can be studied directly. A tetragonal phase model with the chemical formula $PbREF_5$ has been proposed for heavy RE-doped nano-particles in this study. The corresponding space-group *P4/mmm* (NO.123) are proved by quantitative EDS and XRD analyses. Two specific crystalline phases with the same space group have been observed at 460 °C-500 °C and 520 °C-560 °C, respectively. Moreover, a super "pseudo-cubic" cell based on our tetragonal model may give a good explanation to the probable previous cubic-symmetry-misunderstanding by researchers. The RE-doping mechanism is considered to be RE^{3+} replacement of Pb^{2+} as well as interstitial F^- charge compensation. However, unlike the study of heavy RE ions doped systems, core-shell-like structure of pure β-PbF_2 surface absorbed NdF_3 crystals generated after thermal treatment for light RE ions (Nd^{3+}) doped nano-particles. This study has paved a way to more comprehensively understand the properties of the light RE ions doped oxyfluoride glass. The results here would benefit further research on the optical properties and applications of such materials. Recent years, our group has paid much attention on the research of the fabrication of Ln^{3+}-doped nano-particles from oxyfluoride glass by the thermal induction and corrosion treatment, and has done much work on the structural investigations of the obtained nano-particles. In the present and future research, to broaden the application of this material, we will pay much more efforts on the dispersion and surface modification of nano-particles during or after the corrosion process to fabricate the transparent luminescent collosol. And so far, we have made some progress on this work.

http://dx.doi.org/10.5772/57213

Acknowledgements

This work is supported by National Science Fund for Talent Training in Basic Sciences under Grant No.J1103208. The authors are also grateful for the fruitful discussions with Nan Hu, Ming Zhang and Xinxing Zhang.

Author details

Hui Guo[1], Yu Hua[1], Lijuan Zhao[1,2] and Yiming Li[1]

1 The Key Laboratory of Weak-Light Nonlinear Photonics, Ministry of Education, School of Physics, Nankai University, Tianjin, China

2 Applied Physics School of TEDA, Nankai University, Tianjin, China

References

[1] Chatterjee, D. K.; Gnanasammandhan, M. K.; and Zhang, Y. Small Upconverting Fluorescent Nanoparticles for Biomedical Applications, *Small* 2010; 6(24) 2781-2795.

[2] Chen, J.; Guo, C. R.; Wang, M.; Huang, L.; Wang, L. P.; Mi, C. C.; Li, J.; Fang, X. X.; Mao, C. B.; and Xu, S. K. Controllable Synthesis of $NaYF_4$:Yb,Er Upconversion Nanophosphors and their Application to *invivo* Imaging of *Caenorhabditis elegans*, *J. Mater. Chem.* 2011; 21(8) 2632-2638.

[3] Auzel, F. Upconversion and Anti-Stokes Processes with f and d Ions in Solids, *Chem. Rev.* 2004; 104(1) 139-174.

[4] Mai, H. X.; Zhang, Y. W.; Si, R.; Yan, Z. G.; Sun, L. D.; You, L. P.; and Yan, C. H. High-Quality Sodium Rare-Earth Fluoride Nanocrystals: Controlled Synthesis and Optical Properties, *J. Am. Chem. Soc.* 2006; 128(19) 6426-6436.

[5] Kumar, B. R.; Nyk, M.; Ohulchanskyy, T. Y.; Flask, C. A.; and Prasad, P. N. Combined Optical and MR Bioimaging Using Rare Earth Ion Doped $NaYF_4$ Nanocrystals, *Adv. Funct. Mater.* 2009; 19(6) 853-859.

[6] Lin, C. C.; Xiao, Z. R.; Guo, G. Y.; Chan, T. S.; and Liu, R. S. Versatile Phosphate Phosphors $ABPO_4$ in White Light-Emitting Diodes: Collocated Characteristic Analysis and Theoretical Calculations, *J. Am. Chem. Soc.* 2010; 132(9) 3020-3028.

[7] Wang, F.; Han, Y.; Lim, C. S.; Lu, Y. H.; Wang, J.; Xu, J.; Chen, H. Y.; Zhang, C.; Hong, M. H.; and Liu, X. G. Simultaneous Phase and Size Control of Upconversion Nanocrystals Through Lanthanide Doping, *Nature* 2010; 463 1061-1065.

[8] Wang, J. W.; Hao, J. H.; and Tanner, P. A. Upconversion Luminescence of an Insulator Involving a Band to Band Multiphoton Excitation Process, *Opt. Express* 2011; 19(12) 11753-11758.

[9] Haase, M.; and Schäfer, H. Nanopartikel für die Aufwärtskonversion, *Angew. Chem.* 2011; 123(26) 5928-5950.

[10] Wang, Y.; and Ohwaki, J. New Transparent Vitroceramics Codoped with Er^{3+} and Yb^{3+} for Efficient Frequency Upconversion, *Appl. Phys. Lett.* 1993; 63(24) 3268-3270.

[11] Tick, P. A.; Borrellia, N. F.; Cornelius, L. K.; and Newhouse, M. A. Transparent Glass Ceramics for 1300 nm Amplifier Applications, *J. Appl. Phys.* 1995; 78(11) 6367-6374.

[12] Driesen, K.; Tikhomirov, V. K.; Görller-Walrand, C.; Rodríguez, V. D.; and Seddon, A. B. Transparent Ho^{3+}-Doped Nano-Glass-Ceramics for Efficient Infrared Emission, *Appl. Phys. Lett.* 2006; 88(7) 073111.

[13] Tikhomirov, V. K.; Driesen, K.; Görller-Walrand, C.; and Mortier, M. Broadband Telecommunication Wavelength Emission in Yb^{3+}-Er^{3+}-Tm^{3+} Co-Doped Nano-Glass-Ceramics, *Opt. Express* 2007; 15(15) 9535-9540.

[14] Tikhomirov, V. K.; Driesen, K.; and Görller-Walrand, C. Low-Energy Robust Host Heavily Doped with Dy^{3+} for Emission at 1.3 to 1.4 μm, *Phys. Status Solidi A* 2007; 204(3) 839-845.

[15] Mortier, M.; and Patriarche, G. Oxide Glass Used as Inorganic Template for Fluorescent Fluoride Nanoparticles synthesis, *Opt. Mater.* 2006; 28(12) 1401-1404.

[16] Yu, H.; Hu, N.; Wang, Y. N.; Wang, Z. L.; Gan, Z. S.; and Zhao, L. J. The Fabrication of Nano-Particles in Aqueous Solution from Oxyfluoride Glass Ceramics by Thermal Induction and Corrosion Treatment, *Nanoscale Res. Lett.* 2008; 3(12) 516-520.

[17] Lehmann, O.; Kompe, K.; and Haase, M. Synthesis of Eu^{3+}-Doped Core and Core/Shell Nanoparticles and Direct Spectroscopic Identification of Dopant Sites at the Surface and in the Interior of the Particles, *J. Am. Chem. Soc.* 2004; 126(45) 14935-14942.

[18] Hao, S. W.; Sun, L.; Chen, G. Y.; Qiu, H. L.; Xu, C.; Soitah, T. N.; Sun, Y.; and Yang, C. H. Synthesis of Monoclinic Na_3ScF_6:1 mol% Er^{3+}/2 mol% Yb^{3+} Microcrystals by a Facile Hydrothermal Approach, *J. Alloys Compd.* 2012; 522 74-77.

[19] Werts, M. H. V.; Jukes, R. T. F.; and Verhoeven, J. W. The Emission Spectrum and the Radiative Lifetime of Eu^{3+} in Luminescent Lanthanide Complexes, *Phys. Chem. Chem. Phys.* 2002; 4(9) 1542-1548.

[20] Boyer, J. C.; Vetrone, F.; Capobianco, J. A.; Speghini, A.; and Bettinelli, M. Variation of Fluorescence Lifetimes and Judd-Ofelt Parameters between Eu^{3+} Doped Bulk and Nanocrystalline Cubic Lu_2O_3, *J. Phys. Chem. B* 2004; 108(52) 20137-20143.

[21] Cross, A. M.; May, P. S.; Van Veggel F. C. J. M.; and Berry, M. T. Dipicolinate Sensitization of Europium Luminescence in Dispersible 5%Eu:LaF_3 Nanoparticles, *J. Phys. Chem. C* 2010; 114(35) 14740-14747.

[22] Wang, Y. H.; Liu, Y. S.; Xiao, Q. B.; Zhu, H. M.; Li, R. F.; and Chen, X. Y. Eu^{3+} Doped KYF_4 Nanocrystals: Synthesis, Electronic Structure, and Optical Properties, *Nanoscale* 2011; 3(8) 3164-3169.

[23] Kar, A.; and Patra, A. Impacts of Core-Shell Structures on Properties of Lanthanide-Based Nanocrystals: Crystal Phase, Lattice Strain, Downconversion, Upconversion and Energy Transfer, *Nanoscale* 2012; 4(12) 3608-3619.

[24] Hu, N.; Yu, H.; Zhang, M.; Zhang, P.; Wang, Y. Z.; and Zhao, L. J. The Tetragonal Structure of Nanocrystals in Rare-Earth Doped Oxyfluoride Glass Ceramics, *Phys. Chem. Chem. Phys.* 2011; 13(4) 1499-1505.

[25] Yu, H.; Guo, H.; Zhang, M.; Liu, Y.; Liu, M.; and Zhao, L. J. Distribution of Nd^{3+} Ions in Oxyfluoride Glass Ceramics, *Nanoscale Res. Lett.* 2012; 7(1) 275.

[26] Beggiora, M.; Reaney, I. M.; and Islam, M. S. Structure of the Nanocrystals in Oxyfluoride Glass Ceramics, *Appl. Phys. Lett.* 2003; 83(3) 467-469.

[27] Méndez-Ramos, J.; Lavín, V.; Martín, I. R.; Rodríguez-Mendoza, U. R.; Rodríguez, V. D.; Lozano-Gorrín, A. D.; and Núñez, P. Site Selective Study of Eu^{3+}-Doped Transparent Oxyfluoride Glass Ceramics, *J. Appl. Phys.* 2003; 94(4) 2295-2301.

[28] Luo, W. Q.; Wang, Y. S.; Cheng, Y.; Bao, F.; and Zhou, L. H. Crystallization and Structural Evolution of YF_3-SiO_2 Xerogel, *Mater. Sci. Eng. B* 2006; 127(2-3) 218-223.

[29] Yu, H.; Zhao, L. J.; Meng, J.; Liang, Q.; Yu, X. Y.; Tang, B. Q.; and Xu, J. J. Nanocrystal Formation and Structure in Oxyfluoride Glass Ceramics, *Chin. Phys.* 2005; 14(9) 1799-1802.

[30] Yu, H.; Zhao, L. J.; Liang, Q.; Meng, J.; Yu, X. Y.; Tang, B. Q.; Tang, L. Q.; and Xu, J. J. Red Up-Conversion Luminescence Process in Oxyfluoride Glass Ceramics Doped with Er^{3+}/Yb^{3+}, *Chin. Phys. Lett.* 2005; 22(6) 1500-1503.

[31] Lehmann, O.; Kömpe, K.; and Haase, M. Synthesis of Eu^{3+}-Doped Core/Shell Nanoparticles and Direct Spectroscopic Identification of Dopant Sites at the Surface and in the Interior of the particles, *J. Am. Chem. Soc.* 2004; 126(17) 14935-14942.

[32] Méndez-Ramos, J.; Lavín, V.; Martín, I. R.; Rodríguez-Mendoza, U. R.; Rodríguez, V. D.; Lozano-Gorrín, A. D.; and Núñez, P. Role of the Eu^{3+} Ions in the Formation of Transparent Oxyfluoride Glass Ceramics, *J. Appl. Phys.* 2001; 89(10) 5307-5310.

[33] Tikhomirov, V. K.; Furniss, D.; Seddon, A. B.; Reaney, I. M.; Beggiora, M.; Ferrari, M.; Montagna, M.; and Rolli, R. Fabrication and Characterization of Nanoscale, Er^{3+}-Doped, Ultratransparent Oxy-Fluoride Glass Ceramics, *Appl. Phys. Lett.* 2002; 81(11) 1937-1939.

[34] Driesen, K.; Tikhomirov, V. K.; and Görller-Walrand, C. Eu^{3+} as a Probe for Rare-Earth Dopant Site Structure in Nano-Glass-Ceramics, *J. Appl. Phys.* 2007; 102(2) 024312.

[35] Mortier, M.; and Patriarche, G. Structural Characterisation of Transparent Oxyfluoride Glass-Ceramics, J. Mater. Sci. 2000; 35(19) 4849-4856.

[36] Mortier, M.; Goldner, P.; Chateau, C.; and Genotelle, M. Erbium Doped Glass-Ceramics: Concentration Effect on Crystal Structure and Energy Transfer between Active Ions, *J. Alloys Compd.* 2001; 323&324 245-249.

[37] Tyagi, A. K.; Patwe, S. J.; Achary, S. N.; and Mallia, M. B. Phase Relation Studies in $Pb_{1-x}M'_xF_{2+x}$ Systems ($0.0 \leq x \leq 1.0$; M'=Nd^{3+}, Eu^{3+} and Er^{3+}), *J. Solid State Chem.* 2004; 177(4-5) 1746-1757.

[38] Ge, J.; Zhao, L. J.; Guo, H.; Lan, Z. J.; Chang, L. F.; Li, Y. M.; and Yu, H. Structure and Distortion of Lead Fluoride Nanocrystals in Rare Earth Doped Oxyfluoride Glass Ceramics, *Phys. Chem. Chem. Phys*. 2013; 15(40) 17281-17286.

[39] Tikhomirov, V. K.; Mortier, M.; Gredin, P.; Patriarche, G.; Görller-Walrand, C.; and Moshchalkov, V. V. Preparation and Up-Conversion luminescence of 8 nm Rare-Earth Doped Fluoride Nanoparticles, *Opt. Express* 2008; 16(19) 14544-14549.

[40] Silva, M. A. P.; Dantelle, G. ; Mortier, M. ; Monteil, A.; Ribeiro, S. J. L. ; Messaddeq, Y. ; Briois, V. ; and Poulain, M. Local Order Around Rare Earth Ions During the Devitrification of Oxyfluoride Glasses, *J. Chem. Phys.* 2008; 128(24) 244516.

[41] Lavin, V.; Iparraguirre, I.; Azkargorta, J.; Mendioroz, A.; Gonzalez-Platas, J.; Balda, R.; and Fernandez, J. Stimulated and Upconverted Emissions of Nd^{3+} in a Transparent Oxyfluoride Glass-Ceramic, *Opt Mater* 2004; 25 201-208.

[42] Mendez-Ramos, J.; Abril, M.; Martin, I. R.; Rodriguez-Mendoza, U. R.; Lavin, V.; Rodriguez, V. D.; Nunez, P.; and Lozano-Gorrin, A. D. Ultraviolet and Visible Upconversion Luminescence in Nd^{3+}-Doped Oxyfluoride Glasses and Glass Ceramics Obtained by Different Preparation Methods, *J Appl Phys* 2006; 99 113511-113515.